COMMUNICATIONS PHYSICS

ARTICLE

https://doi.org/10.1038/s42005-019-0161-5 OPEN

Operation of graphene magnetic field sensors near the charge neutrality point

Guibin Song[1], Mojtaba Ranjbar[1] & Richard A. Kiehl[1]

Graphene is a promising material for sensing magnetic fields via the Hall effect due to its atomic-scale thickness, ultra-high carrier mobilities and low cost compared to conventional semiconductor sensors. Because of its Dirac band structure, graphene sensors differ from semiconductor sensors in that both electrons and holes participate in the carrier transport. This two-channel transport complicates the sensor operation and causes performance trade-offs that demand careful examination. Here, we examine the operation of graphene sensors operated near the charge neutrality point (CNP) where two-channel transport prevails. We find that, while the largest magnetoresistance occurs exactly at the CNP, the maximum realizable Hall sensitivities occur away from the CNP and depend on linearity constraints and power limitations. In particular, a more stringent linearity constraint reduces the realizable sensitivities for mobilities above a critical value μ_c, which scales with magnetic field.

[1] School of Electrical, Computer and Energy Engineering, Arizona State University, Tempe, AZ 85287, USA. Correspondence and requests for materials should be addressed to R.A.K. (email: Richard.Kiehl@asu.edu)

Graphene is a promising material for magnetic field sensors because of its fundamental advantages of high carrier mobility, low sheet carrier density and weak temperature dependence[1–5], and its practical advantages of simple and low-cost fabrication processes[5–9]. Studies of graphene for both magnetoresistance (MR)[10–12] and Hall sensors[2,3,13] have demonstrated performance outpacing traditional magnetic sensors based on semiconductors. For example, a large MR of ~2000% at 9 T has been demonstrated in multilayer graphene on hexagonal boron nitride (h-BN)[12]. An even larger MR of 55,000% at 9 T was obtained in extraordinary magnetoresistance devices, where the geometrical MR is enhanced by an embedded metal structure[10,11]. A record value of current-related sensitivity S_I of 5700 $VA^{-1}T^{-1}$ has been reported[2] for a graphene Hall sensor, which is nearly two orders of magnitude higher than that of commercial Silicon Hall sensors (~100 $VA^{-1}T^{-1}$)[14] and twice as high as that for the best two-dimensional electron gas (2DEG) based Hall sensors[15]. This record value was achieved in a structure comprised of exfoliated graphene and h-BN stacks designed for high mobility. S_I values in the range of about 1000–3000 $VA^{-1}T^{-1}$ have been reported for more practical structures based on chemical vapor deposition (CVD) deposited graphene transferred onto various insulators, including exfoliated h-BN[2], CVD h-BN[6], and SiO_2[3,5]. Advanced "encapsulated" designs based on an all-CVD h-BN/graphene/h-BN sandwich structure have also been reported[8], but have been limited thus far to about 100 $VA^{-1}T^{-1}$ due to high carrier densities, emphasizing the importance of obtaining low carrier density, in addition to high mobility, for high sensitivity.

The MR, sensitivity and linearity of graphene sensors are closely related to the presence of both electrons and holes near the charge neutrality point (CNP). The existence of a CNP is a unique feature of graphene's Dirac band structure and distinguishes graphene sensors from conventional semiconductor based sensors. Despite the general interest and demonstrated promise of graphene-based sensors, there has been little detailed investigation of the magnetoresistance characteristics and sensor performance of graphene near the CNP, which is essential for optimizing graphene sensor operation.

Here we present a study of the potential performance and optimization of graphene-based MR and Hall sensors. The study is based on a two-channel model that combines the longitudinal and Hall resistivities of parallel electron and hole channels with electrostatic carrier density expressions for graphene. Our primary focus is the optimization at biases near the CNP (i.e., the Dirac point), where the transport is complicated by the presence of both electrons and holes. We begin by validating our model by examining the experimental characteristics of sensors based on commercial CVD graphene transferred to a SiO_2/p-Si substrate over wide ranges of gate-bias V_g, magnetic field B, and temperature T. We show that the experimental MR–B, Hall resistivity ρ_{xy}–B and ρ_{xy}–V_g characteristics are well-described by the model, including nonlinearities and unusual gate-bias dependence in the ρ_{xy}–V_g characteristic near the CNP. We use the model to extract carrier mobilities and densities and show that model agrees with experimental data over wide ranges in gate bias and magnetic field. The characteristics are also examined over a wide temperature range (10–300 K). We then make use of the validated model to study the optimization of the sensitivity, linearity, and MR and to estimate the realizable performance in high-quality graphene. Of particular interest in our results are trade-offs due to the linearity constraints of an application, which are especially important at high mobilities and high magnetic fields—a regime mostly neglected in prior work.

Results

Model. Two-carrier magnetoresistance expressions were used to analyze the experimental data and predict optimized performance. For a single carrier, longitudinal resistivity ρ_{xx} and Hall resistivity ρ_{xy} are given by:

for electrons,

$$\rho_{xx} = \frac{1}{en\mu_e}, \tag{1}$$

$$\rho_{xy} = \frac{B}{en}; \tag{2}$$

for holes,

$$\rho_{xx} = \frac{1}{ep\mu_h}, \tag{3}$$

$$\rho_{xy} = \frac{B}{ep}; \tag{4}$$

where e is the elementary charge and n, p, μ_e, μ_h represent carrier densities and mobilities for electrons and holes, respectively. For parallel electron and hole channels with equal mobilities, ρ_{xx} and ρ_{xy} are given by:

$$\rho_{xx} = \frac{1}{e}\frac{(p+n)\left(1+(\mu B)^2\right)}{\mu\left((p+n)^2+(\mu B)^2(p-n)^2\right)}, \tag{5}$$

$$\rho_{xy} = \frac{1}{e}\frac{B(-p+n)(1+(\mu B)^2)}{\left((p+n)^2+(\mu B)^2(p-n)^2\right)}. \tag{6}$$

Expressions for unequal mobilities are given by Gopinadhan et al.[12]. While for a single carrier ρ_{xx} is independent of B, Eq. (5) shows that ρ_{xx} is dependent on B^2 for two carriers of comparable density. Therefore, a large MR is possible near the CNP. While for a single carrier ρ_{xy} depends linearly on B and tends to infinity as the carrier density approaches zero, Eq. (6) shows that ρ_{xy} depends nonlinearly on B for two carriers of comparable density and tends to zero as the net carrier density approaches zero. Therefore, the linearity and sensitivity of a graphene Hall sensor are strongly influenced by two-carrier transport.

For simplicity in discussing the model, we have given the expressions in the case of $\mu_e = \mu_h$ in Eqs (5) and (6), whereas the expressions for unequal mobilities[12] were used in the fitting analysis presented later (Figs. 1–4). Examination of the expressions for unequal mobilities reveals that the deviations from the single carrier case occur when the two channels have comparable conductivities[12], not comparable densities. Nevertheless, the deviations occur near the CNP even for unequal mobilities due to the strong dependence of carrier densities on gate bias. Near the CNP, inhomogeneities may occur due to charge impurities, intrinsic structural wrinkles, and substrate roughness[1,16]. It is believed that the resulting random potential fluctuations in the channel modulate the Dirac band structure so strongly that interspersed electron and hole puddles form, as has been observed experimentally[17,18]. Various theoretical treatments have been proposed to provide a detailed understanding of transport in this situation[1,19–21]. A simple physical picture[21,22] is that the carriers move along percolation paths while scattering from puddle interfaces. Since the puddles are larger than the mean free path, the conductivities of individual puddles can be described by drift-diffusion[21], and the transport involves a longer effective path-length and additional scattering (higher resistance). Thus, although puddles complicate the physical picture at the CNP and modify the effective transport parameters, the two-channel model still provides a useful approximation and has been

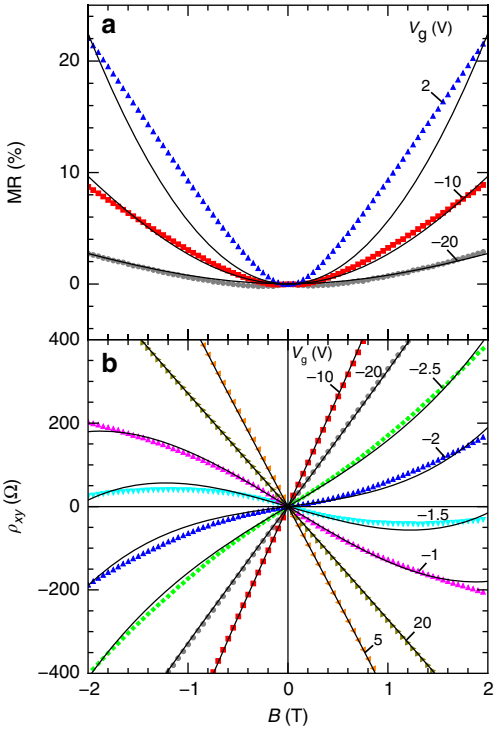

Fig. 1 Comparison of experimental and modeled results. Dependence of magnetoresistance MR and Hall resistivity ρ_{xy} on magnetic field B for various values of gate-bias V_g: **a** MR–B and **b** ρ_{xy}–B. Good agreement is obtained between the experiment (dots) and model (solid lines) over wide ranges in V_g and B. (The current and temperature for these and the other experiments were 1 μA and 100 K, respectively, unless stated otherwise.)

used successfully for the study of graphene sensors by several groups[3,12,19].

To develop a simple theory (i) for checking the accuracy of the electron and hole densities extracted from the data in our analysis and (ii) for predicting the performance of MR and Hall sensors, we combined the two-carrier magnetoresistance expressions[12] with electrostatic carrier density expressions[23] for the gate-bias dependent electron and hole carrier densities in graphene, similar to that done by Chen et al.[3]. The key relationships in the electrostatic carrier density expressions are:

$$n_{\mathrm{tot}} = p + n \cong \sqrt{n_0^2 + n[V_g]^2}, \tag{7}$$

$$n\left[V_g\right] = p - n = -\frac{C_{\mathrm{ox}}}{e}(V_g - V_{\mathrm{CNP}}) \tag{8}$$

where n_{tot} is the total carrier density, n_0 is the minimum carrier density at the CNP, $n\left[V_g\right]$ is the gate-bias dependent net charge density, C_{ox} is the gate capacitance and V_{CNP} is the gate bias at the charge neutrality point. In contrast to Chen et al.[3], who used a simplified model assuming that $\mu B \ll 1$, we use the full two-carrier resistivity equations above. This allows us to study performance trade-offs due to linearity constraints and to predict the sensor performance for high-quality graphene (high μ and low n_0) and high magnetic fields.

Comparison of experimental and modeled results. Figure 1a shows the variation of the MR, which is defined as $\{\rho_{xx}(B) - \rho_{xx}(0)\}/\rho_{xx}(0)$, as a function of magnetic field B for different gate biases V_g. The current and temperature for these and the other experiments were 1 μA and 100 K, respectively, unless stated otherwise (see Supplementary Note 1 and Supplementary Fig. 1 for 300 K results). For the biases farthest from the CNP ($V_g = -20$ V), where one carrier dominates, the MR is very small as expected from the Drude model of single carrier transport. It can be seen that the highest MR is achieved at V_g close to the CNP ($V_g = -2$ V), where both carriers are present. The MR at 2 T and 100 K is ~22%, which is comparable with that previously reported for graphene at the same field and temperature[12].

The solid lines in Fig. 1a present the calculated MR using the two-channel model. It is important to note here that the calculated MR agrees well with the experimental data, except that the experimental data is more linear at high fields. Such linearity has been attributed to electron-hole recombination leading to an edge conductivity contribution[24,25] as well as to the existence of electron and hole puddles[20].

A highly linear ρ_{xy}–B characteristic is critical for many Hall sensor applications. Figure 1b shows the Hall resistivity ρ_{xy}–B at various V_g. It can be seen that the linearity of ρ_{xy} degrades when the gate bias is close to the CNP ($V_g = -2.5$, -2, -1.5, and -1 V). Following Xu et al.[5], linearity error α is defined as $(\rho_{xy} - \rho_{xy}^0)/\rho_{xy}^0$, where ρ_{xy}^0 is the best linear fit value of the ρ_{xy}–B curve. We define α_{max} as the maximum of α over the B range. In the electron or hole dominated regimes ($V_g = -20$ and 20 V), the value of α_{max} for our data is very low, <2%. However, α_{max} increases rapidly as V_g approaches the CNP, reaching a value of 77% at $V_g = -2$ V, which is much too high for Hall sensor applications. This large α_{max} means that ρ_{xy} is not linearly dependent on B in the two-carrier regime.

Close examination of the dependence of the ρ_{xy}–B characteristic on V_g shown in Fig. 1b reveals another type of unusual behavior near the CNP. The rotation of the curves around the origin with increasing V_g changes direction near the CNP—i.e., the rotation is clockwise near the CNP (the slope ρ_{xy}/B decreases with V_g from −10 to +5 V) while it is counter-clockwise away from the CNP (the slope ρ_{xy}/B increases with V_g for $|V_g| > \sim 10$ V). In the analysis below, it will be shown that this unusual rotation reversal behavior is also a result of two-carrier transport.

If there are two distinct carrier species—either (i) two carriers of the same type (both electrons or both holes) with different mobilities or (ii) two carriers of different type (one electrons, the other holes) with the same (or different) mobilities—then each species has a different contribution to the overall MR–B and ρ_{xy}–B characteristics. To examine whether the nonlinearity and rotation effects in Fig. 1b can be explained by two-carrier transport, we fit the MR–B and ρ_{xy}–B experimental data in Fig. 1a, b simultaneously with the two-carrier magnetoresistance expressions in Eqs (5) and (6). The fitting parameters were the electron and hole mobilities, which were taken to be independent of V_g, and the carrier densities, which were taken to be dependent on V_g. This fitting procedure allows us to extract density and mobility values for the electrons and holes.

Calculated results for the two-channel model using the extracted parameters are in close agreement with the experimental results, as shown in Fig. 1. The accuracy of the theory is shown by the good agreement between the experimental and modeled resistivity curves in Fig. 1. However, the validity of our model also requires that the extracted mobilities and densities are accurate. The extracted electron and hole mobilities are 2598 and 2168 $\mathrm{cm^2\,V^{-1}\,s^{-1}}$, respectively, which are reasonable values for commercial quality graphene on SiO_2/p-Si substrates. It is also important to examine the extracted carrier densities in order to validate our model. While the extraction of carrier density from Hall data is simple for a single charge carrier, the presence of two carriers makes the extraction difficult. Nevertheless, we find that the extracted values of electron and hole density are also reasonable throughout the entire gate-bias range, as shown in Fig. 2. (The theoretical curves in Fig. 2 will be discussed later.)

Here we experimentally examine the influence of two-carrier transport on the Hall sensitivity. The current-related sensitivity S_I is defined as $V_{xy}/IB = \rho_{xy}/B$[14]. Two-carrier transport near the CNP will affect S_I through its impact on the ρ_{xy}–V_g characteristic. The variation of ρ_{xx}, ρ_{xy}, and S_I with V_g is shown in Fig. 3. The increase in ρ_{xx} with increasing B near the CNP shown in Fig. 3a is due to two-carrier transport. Figure 3b shows that $|\rho_{xy}|$ peaks on either side of the CNP and that ρ_{xy} crosses zero at the CNP. This is different from the case of a single carrier, where ρ_{xy} is proportional to the inverse of the carrier density and therefore tends to infinity as the carrier density approaches zero. In graphene, however, the total carrier density $(p + n)$ does not approach zero. Instead, $(p + n)$ reaches a minimum value n_0 and the net density $(p - n)$ changes sign at the CNP. This peaking of $|\rho_{xy}|$ places an important limitation on the realizable sensitivity and affects the optimum bias condition for a graphene Hall sensor, as will be considered in detail later. While the temperature for the data presented in this paper was 100 K, the ρ_{xx}–V_g and ρ_{xy}–V_g characteristics were examined over a range in temperature from 10 to 300 K and confirm the excellent thermal stability of graphene Hall sensors[5] (see Supplementary Note 2 and Supplementary Fig. 1).

It is also interesting to note that the S_I behavior in Fig. 3c indicates that ρ_{xy}/B decreases with increasing V_g near the CNP (V_g from −7 to +5 V) while it increases with increasing V_g away from the CNP, which is consistent with our conclusion that the rotation reversal in Fig. 1b is the result of two-carrier transport.

To test the capability of our model for predicting MR and Hall sensor performance, we attempted to fit our experimental data over wide ranges in gate voltage and magnetic field. Following Peng et al.[3], n_0 was extracted by fitting the S_I –V_g characteristic in Fig. 3c. The extracted $n_0 = 4.65 \times 10^{11}$ cm^2 was then used to calculate the electron and hole densities as a function of V_g using the electrostatic carrier density expressions in Eqs (7) and (8). The calculated densities are plotted along with the experimental values in Fig. 2 and are seen to be in good agreement with the experiment. From the calculated densities and extracted mobilities, we worked backward to calculate theoretical ρ_{xy}–V_g characteristics for various B, which are plotted along with the experimental data in Fig. 3b. Working backward in a similar way, the theoretical MR, S_I, and α_{max} characteristics were determined and found to be in good agreement with experimental results, as shown in Fig. 4a–c, respectively. The agreement between the theory and experiment in Figs. 3b and 4b is excellent, except near the peak on the electron-side. (The better agreement on the hole side of the characteristics simply reflects the better fit obtained on the hole side in Fig. 2.) The agreement shows that our model should be useful for estimating the optimized performance of graphene Hall sensors over wide ranges in mobility and magnetic field.

Realizable sensitivities. We now use our model to explore the influence of material-quality parameters (μ and n_0) on sensitivity, linearity, and MR for graphene magnetic sensors.

Figure 5a, b shows modeled results for n_0 over the range 6.1×10^{10}–1×10^{12} cm^{-2} with μ and B set equal to 2000 cm^2 V^{-1} s^{-1} and 2 T, respectively. (The lower limit of n_0 was chosen to be equal to the theoretical thermal limit at 300 K[3].) It is seen that n_0 has a strong influence on the peak value of S_I, which occurs at about 1 V on either side of the CNP and reaches a value of 5360 VA^{-1} T^{-1} as n_0 decreases to 6.1×10^{10} cm^{-2}. As depicted in Fig. 5c, the peak S_I is proportional to $1/n_0$, which agrees with Chen et al.'s conclusion in previous work[3]. The peak value of α_{max} occurs exactly at the CNP and reaches a value 8.8% independent of n_0, while the width of the α_{max} decreases with decreasing n_0.

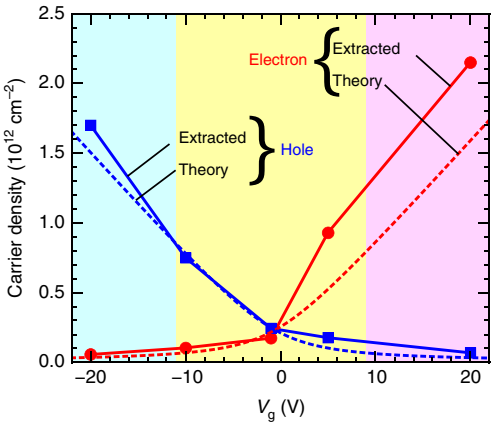

Fig. 2 Comparison of experimental and calculated carrier densities. The extracted densities (solid) and calculated densities (dashed) as a function of gate-bias V_g are in good agreement with each other, which is important for validation of our model. The color bands in this figure indicate hole dominated (light blue), electron dominated (pink), and two-carrier (yellow) regions

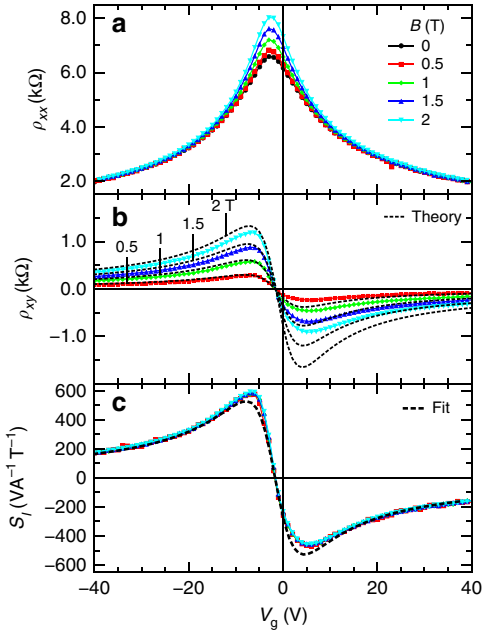

Fig. 3 Gate-bias V_g dependence of resistivity and sensitivity. **a** Longitudinal resistivity ρ_{xx}-V_g and **b** Hall resistivity ρ_{xy}-V_g and **c** the current-related sensitivity S_I-V_g for various magnetic field B. The dashed lines in (**b**) are theoretical characteristics calculated from the model, which show good agreement with the experiment, especially on the left side of the CNP. The dashed line in (**c**) shows the fit to the data that was used to extract the residual carrier density n_0 used in our model. The peaking of $|\rho_{xy}|$ places a limitation on sensitivity and affects the optimum bias condition

Since α_{max} is proportional to $(\mu B)^2$[14], the linearity is improved at lower B. Thus, both higher sensitivity and higher linearity occur for lower n_0. At this moderate mobility, α_{max} is always low enough that operation at the peak S_I point is possible. However, for high mobilities the strong variation in both S_I and α_{max} with V_g introduces an important performance trade-off, which we examine next.

Figure 5d, e shows results for μ over the range of 1000–20,000 cm^2 V^{-1} s^{-1} for n_0 and B set equal to

1×10^{11} cm^{-2} and 2 T, respectively. It is seen that the peak values of both S_I and α_{max} increase with increasing μ. Since increased S_I is beneficial while increased α_{max} is not, this represents a performance trade-off. Because of this trade-off, the peak S_I cannot be realized and is limited to a value that depends on the α_{max} constraint; we call this realizable value S_I^R. For example, if α_{max} is constrained to 10% and $\mu = 2000$ cm^2 V^{-1} s^{-1}, then Fig. 5d shows that S_I^R occurs at 1.3 V (square symbol), which is the peak of S_I and is equal to 3270 VA^{-1} T^{-1}. On the other hand, for the same α_{max} but μ equal to 20,000 cm^2 V^{-1} s^{-1}, S_I^R occurs at 3.7 V (triangle symbol), which is away from the peak S_I, and is therefore limited to only 2180 VA^{-1} T^{-1}. At this operating point, $|S_I|$ is only about 20% of its peak value of 9730 VA^{-1} T^{-1}. The reason behind this counterintuitive effect (viz., that increased mobility can degrade S_I^R) and its implications will be considered later.

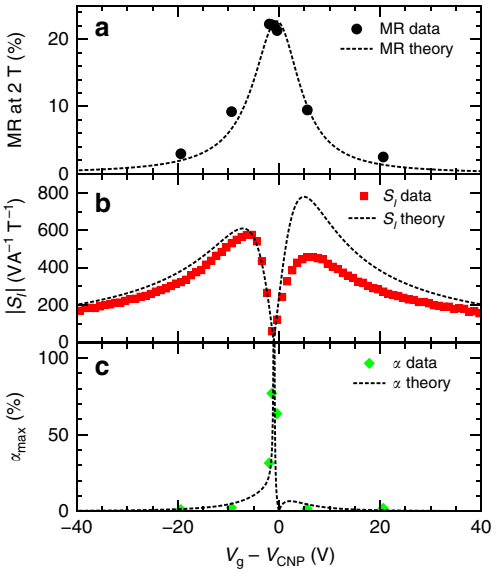

Fig. 4 Comparison of experiment and theory. **a** Magnetoresistance MR, **b** current-related sensitivity $|S_I|$, and **c** maximum linearity error α_{max} as a function of gate-bias $V_g - V_{CNP}$. V_{CNP} is the charge neutrality point

In the above examples, the electron and hole mobilities were assumed to be equal. Figure 5f, g shows results for carrier mobility ratios μ_h/μ_e over the range of 1 to 1/10. As can be seen from Fig. 5f, g, decreasing μ_h while keeping μ_e constant causes the peak S_I to increase and shift to the left while α_{max} decreases near the peak (both desirable). In the case of $\mu_h/\mu_e = 1000/5000$, for example, the peak S_I is about two times that for equal mobilities while the α_{max} at the peak is 1% compared with 22% for equal mobilities. These changes in the S_I and α_{max} characteristics result in an improvement in S_I^R of nearly three times that for $\alpha_{max} = 10\%$ (see symbols in Fig. 5f). The reason for this improvement is that the transport for a higher mobility ratio is more similar to that for a single carrier, where S_I tends to be high while α_{max} is low. It is interesting that a difference in carrier mobilities can have a significant influence on both S_I and α_{max} as well as the optimum V_g bias point. The impact of this on performance will also be considered in a later section.

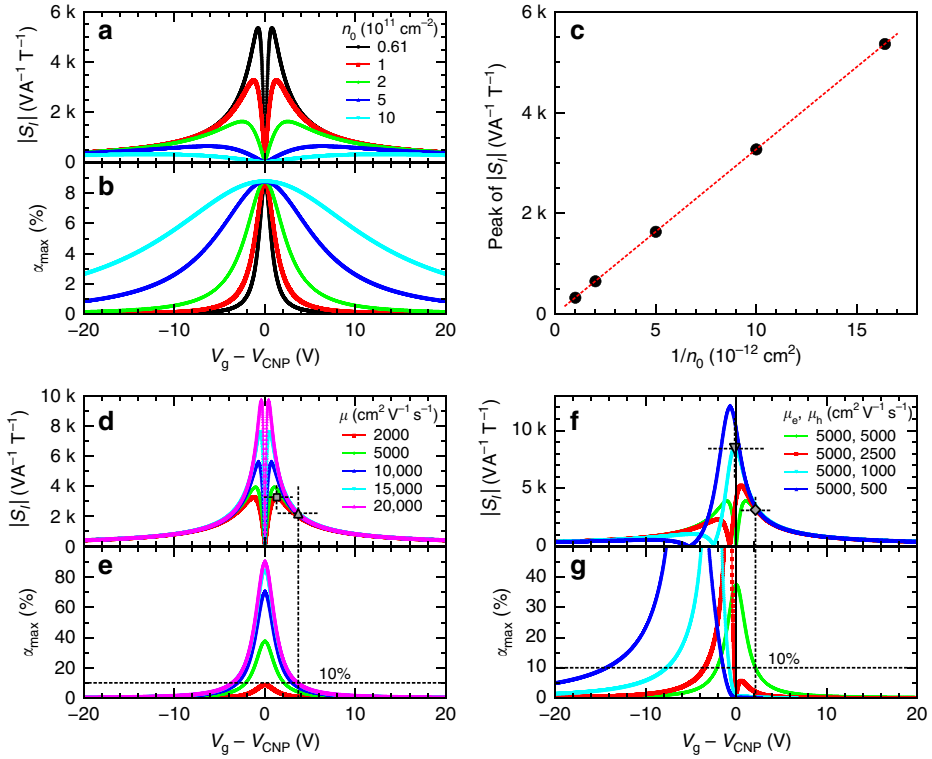

Fig. 5 The influence of material-quality parameters on sensitivity and linearity. **a** Modeled current-related sensitivity $|S_I|$ and **b** maximum linearity error α_{max} vs $V_g - V_{CNP}$ at various minimum carrier density n_0 for mobility $\mu = 2000$ cm^2 V^{-1} s^{-1}, magnetic field $B = 2$ T. **c** $|S_I|$ vs $1/n_0$, as extracted from (**a**). **d** modeled $|S_I|$ and **e** α_{max} vs $V_g - V_{CNP}$ for equal electron and hole mobilities ($\mu_e = \mu_h = \mu$). **f** modeled $|S_I|$ and **g** α_{max} vs $V_g - V_{CNP}$ for unequal electron and hole mobilities ($\mu_e \neq \mu_h$) for $n_0 = 1 \times 10^{11}$ cm^{-2}, $B = 2$ T. V_g is the gate bias and V_{CNP} is the charge neutrality point. Symbols in (**c**) and (**d**) show the realizable S_I for $\alpha_{max} = 10\%$ for different mobilities. The modeling shows that the realizable S_I values, which are inversely proportional to n_0, are reduced by linearity constraints

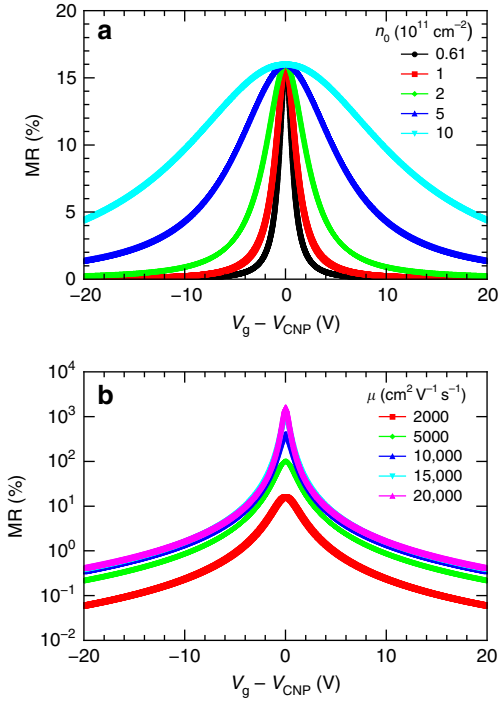

Fig. 6 The influence of material-quality parameters on magnetoresistance. **a** Modeled magnetoresistance MR vs gate-bias $V_g - V_{CNP}$ at various minimum carrier density n_0 for mobility $\mu = 2000\ \mathrm{cm^2\ V^{-1}\ s^{-1}}$, magnetic field $B = 2$ T and **b** modeled MR vs $V_g - V_{CNP}$ for various mobilities ($\mu_e = \mu_h = \mu$) for $n_0 = 1 \times 10^{11}\ \mathrm{cm^{-2}}$, $B = 2$ T. V_{CNP} is the charge neutrality point. The modeling shows that the key to achieving a high MR in graphene is having a high μ, rather than a low n_0

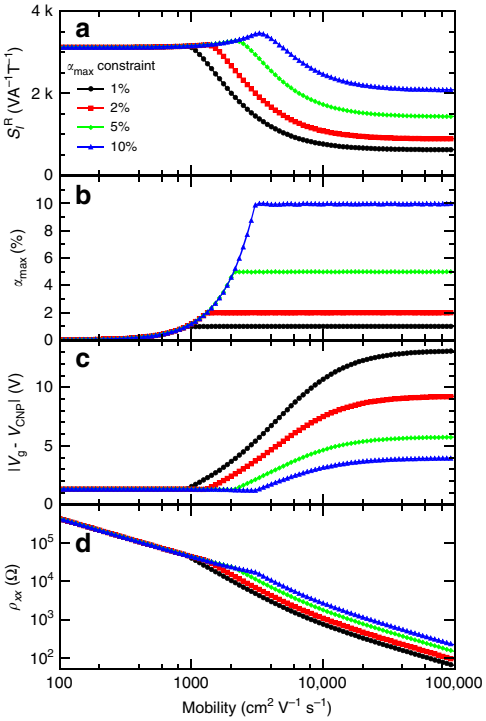

Fig. 7 Dependence of realizable current-related sensitivity on mobility and linearity. Modeled **a** realizable current-related sensitivity S_I^R, **b** maximum linearity error α_{max}, **c** $|V_g - V_{CNP}|$, and **d** longitudinal resistivity ρ_{xx} vs mobility for various α_{max} constraints for $n_0 = 1 \times 10^{11}\ \mathrm{cm^{-2}}$ and $B = 2$ T. Gate-bias V_g is optimized for the highest S_I^R within the α_{max} constraints. V_{CNP} is the charge neutrality point. These results show the interplay between the linearity constraint and mobility in determining the realizable S_I values; in particular a stringent linearity constraint together with a high mobility results in a substantial reduction in S_I^R

We have also used our model to explore how the MR is affected by μ and n_0. Figure 6a shows the modeled results for MR–V_g when n_0 is varied from 6.1×10^{10} to $1 \times 10^{12}\ \mathrm{cm^{-2}}$ with μ and B set equal to $2000\ \mathrm{cm^2\ V^{-1}\ s^{-1}}$ and 2 T, respectively. Contrary to what was seen for S_I in Fig. 5a, the peaks of MR occur exactly at the CNP. While the peak MR value is independent of n_0, a larger n_0 gives a wider peak and hence a larger V_g operating range. Figure 6b shows the calculated MR for μ varied from 1000 to $20{,}000\ \mathrm{cm^2\ V^{-1}\ s^{-1}}$ with n_0 and B set equal to $1 \times 10^{11}\ \mathrm{cm^{-2}}$ and 2 T, respectively. The MR peak value increases dramatically with μ, reaching nearly 1600% as μ approaches $20{,}000\ \mathrm{cm^2\ V^{-1}\ s^{-1}}$, a mobility representative of that for high-quality graphene on h-BN[26,27]. Figure 6a, b shows that, in contrast to Hall sensitivity, the key to achieving high MR in graphene is having a high μ rather than a low n_0.

Here we examine the details of how a linearity constraint influences the realizable current-related sensitivity S_I^R, as well as the absolute sensitivity $S_A = V_{xy}/B = S_I\ I$. S_A is proportional to $(\mu/n_s)^{1/2}P^{1/2}$[14], where n_s is sheet carrier density and P is power, and thus S_A is the most important parameter for power-limited applications. The realizable value of S_A, which we refer to as S_A^R, is constrained by both the needed linearity and the power limitation for the particular application. The linearity constraint affects the S_I^R at high mobility values, as illustrated in Fig. 7a, b, which show S_I^R and α_{max} vs μ at $B = 2$ T for various constraints on α_{max} (1, 2, 5, and 10%). As shown in Fig. 7b, the α_{max} constraint is active for mobilities above a critical value, which we define as μ_c. For example, the value of μ_c for $\alpha_{max} = 10\%$ is $3270\ \mathrm{cm^2\ V^{-1}\ s^{-1}}$. It can be seen in Fig. 7a that S_I^R is near its maximum value of 3470 $\mathrm{VA^{-1}\ T^{-1}}$ when μ is less than about $1000\ \mathrm{cm^2\ V^{-1}\ s^{-1}}$ for all shown values of α_{max}. However, increasing the mobility above $1000\ \mathrm{cm^2\ V^{-1}\ s^{-1}}$ results in an α_{max}-dependent decrease in S_I^R. This is because the operating bias must be moved further away from the CNP to meet the α_{max} constraint when $\mu > \mu_c$, as is shown in Fig. 7c. While S_I^R barely changes when μ is lower than $1000\ \mathrm{cm^2\ V^{-1}\ s^{-1}}$, the channel resistivity ρ_{xx} at the operating bias increases rapidly with decreasing μ to values too high for low-power operation, as illustrated in Fig. 7d. At a higher resistivity the maximum current I_{max} is power-limited at a lower value. Although S_I^R is commonly used as a figure of merit of Hall sensors, S_I^R does not take power into account. Thus, S_A^R, which depends on both linearity constraints and power limitations, is a better figure merit for power-limited applications. Figure 8a, b shows S_A^R and α_{max} vs μ for various α_{max} constraints values (1, 2, 5, 10%; and unconstrained) with an assumed power limitation of 1 mW. In contrast to S_I^R, which decreases for higher mobilities, we can see that S_A^R increases monotonically with μ. However, the linearity constraints greatly reduce S_A^R compared with the unconstrained case in the high mobility regime when $\mu > \mu_c$. For example, the value of μ_c for $\alpha_{max} = 10\%$ is $4040\ \mathrm{cm^2\ V^{-1}\ s^{-1}}$. At $\mu = 20{,}000\ \mathrm{cm^2\ V^{-1}\ s^{-1}}$, for instance, α_{max} constraints of 1 and 10% lead to reductions of S_A^R by 58% and 27%, respectively, compared with the unconstrained value. The results in Fig. 8a show that an S_A^R of 4.5 $\mathrm{VT^{-1}}$ at 1 mW (equivalent 0.14 $\mathrm{VT^{-1}}$ at 1 μW) should be possible for high-quality graphene with good linearity over a large magnetic field range ($\alpha_{max} = 10\%$, $B = 2$ T, $n_0 = 1 \times 10^{11}\ \mathrm{cm^{-2}}$, $\mu = 100{,}000\ \mathrm{cm^2\ V^{-1}\ s^{-1}}$).

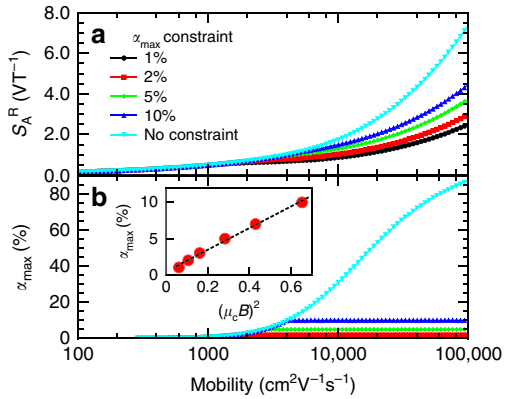

Fig. 8 The dependence of realizable absolute sensitivity on mobility and linearity. **a** Modeled realizable absolute sensitivity S_A^R and **b** maximum linearity error α_{max} vs mobility for various α_{max} constraints for minimum carrier density $n_0 = 1 \times 10^{11}$ cm^{-2}, magnetic field $B = 2$ T and power $P =$ 1 mW. Gate-bias V_g is optimized for the highest S_A^R within the α_{max} constraints. The inset shows the dependence of α_{max} on $(\mu_c B)^2$, where the critical mobility μ_c is determined from the break points in (**b**) and the dashed line is a linear fit. The results show that, when mobility is higher than μ_c, the linearity constraints substantially reduce S_A^R compared with the unconstrained case

Discussion

Several points about the results presented above deserve further discussion. As was seen in the calculations, higher mobility and higher magnetic field result in poorer linearity, which limits S_I^R and S_A^R to lower values. Since α_{max} is proportional to $(\mu B)^2$[14], the calculated results for $B = 2$ T in Figs. 5–8 can easily be extended to other B values. In the insert of Fig. 8b we have plotted α_{max} vs $(\mu_c B)^2$, as determined from the data in Fig. 8. As shown in Fig. 8, α_{max} is <10% for $(\mu_c B)^2 < 0.65$, which means that S_A^R is not limited by a 10% linearity constraint; while for larger $(\mu B)^2$, S_A^R is reduced for a 10% linearity constraint. Thus, determining μ_c (the mobility above which the realizable sensitivity is constrained by linearity) for the α_{max} and B required by a particular application can be useful in designing graphene Hall sensors. This is obviously important when both the mobility and magnetic field are high. It is important to note that the nonlinearities are also significant in the mT range when the mobility is very high, as is possible in optimized graphene devices. For example, for a mobility of 100,000 cm^2 V^{-1} s^{-1}, $(\mu B)^2$ is equal to 1 at 100 mT and α_{max} is over 10% (see inset of Fig. 8b), and the nonlinearity cannot be neglected. Thus, the linearity constraints discussed in this paper can also be important for low fields used in many Hall sensor applications.

As was seen in Fig. 7a, S_I^R is near its maximum value for μ below about 1000 cm^2 V^{-1} s^{-1}. This does not mean that a low mobility is sufficient for good sensor performance since power limits must also be considered in many applications. S_A^R is the relevant figure-of-merit for power-limited applications and lower mobility limits S_A^R to lower values. The advantage of graphene for achieving high S_A^R is that it offers both high mobility and low sheet carrier density. For example, for a simple graphene-on-SiO$_2$ structure with μ and n_0 values of 7800 cm^2 V^{-1} s^{-1} and 1×10^{11} cm^{-2} [3], respectively, the equivalent S_A^R value based on the reported S_I and current–voltage data is 0.9 VT^{-1} at a power of 1 mW with a linearity error of 4% for $B = 0.4$ T. This S_A^R value, which is slightly lower than our calculated value of 1.4 VT^{-1} for the same parameters, is the best reported result for this simple structure. For an advanced h-BN encapsulated, exfoliated graphene[2] structure, record sensitivity values of voltage-related sensitivity $S_V = 2.8$ T^{-1} and $S_I = 5700$ VA^{-1} T^{-1} have been reported, which correspond to an equivalent S_A^R value of 4.0 VT^{-1} at 1 mW. Although neither the linearity nor the mobility were reported with this record data, we can use our model to estimate the sensitivity and linearity by assuming $\mu = 80{,}000$ cm^2 V^{-1} s^{-1} (the mobility reported for similar h-BN encapsulated CVD graphene[26]) and $n_0 = 1 \times 10^{11}$ cm^{-2} (a typical value for high-quality graphene). Our model shows that an equivalent S_A^R of 4.0 VT^{-1} at 1 mW should be possible with $\alpha_{max} = 10\%$ for B up to 2 T. If we increase μ to 120,000 cm^2 V^{-1} s^{-1}, the best value reported near room temperature in exfoliated and suspended graphene[28], then S_A^R increases by about 20% to 4.9 VT^{-1} at 1 mW. Thus, our model indicates that the record experimental S_A^R reported for advanced graphene Hall structures is 80% of what can be achieved with good linearity ($\alpha_{max} = 10\%$). If excellent linearity ($\alpha_{max} = 1\%$) is required, however, our model indicates that an S_A^R value of 2.8 VT^{-1} at 1 mW is the best that can be expected.

An important part of this study has been to take into account how the linearity constraint of an application influences the achievable performance of a graphene Hall sensor. The basic issue is that, even though graphene offers high mobility with low residual carrier density at biases near the CNP (both beneficial for Hall sensing), linearity is reduced because of comparable conductivities for the electron and hole channels in this bias regime. Thus, schemes for providing that one channel conductivity dominates over the other could be useful for improving linearity. The obvious approach of biasing the device away from the CNP so that the density of one carrier dominates can improve linearity, but seriously degrades sensitivity due to the increased carrier density. However, the alternative scheme of reducing the mobility of one carrier compared to the other does not suffer from this drawback. While electron and hole mobilities in graphene are usually similar, carrier mobility ratios of ~0.3 have been reported for graphene FETs[29,30] and attributed to asymmetric scattering for electrons and holes[30]. Higher ratios might be possible in engineered structures. Calculated results on the effect of the mobility ratio μ_h/μ_e on Hall sensor sensitivity and linearity were presented in Fig. 5d, where it can be seen that S_I^R improves by a factor of nearly 3 for $\mu_h/\mu_e = 0.2$ and $\alpha_{max} = 10\%$. In the power-limited case, our calculations show that an improvement in S_A^R of about 50% is possible under the same assumptions. Another scheme for providing that one conduction channel dominates over the other is to use an electrical contact technology having different contact resistances for electrons and holes. Previous studies have reported electron-hole conduction asymmetry for various metal/graphene contacts[31–33], and this effect might also be engineered to improve Hall sensor linearity.

It is important to realize that although the two-carrier nature of graphene is a disadvantage for linearity, this does not mean that graphene is inferior to single-carrier semiconductor Hall sensors. Our calculations for graphene with $n_0 = 1 \times 10^{11}$ cm^{-2} give an S_I^R of 3470 VA^{-1} T^{-1} with 10% linearity, which is comparable with the best experimental S_I^R value of 2745 VA^{-1} T^{-1} reported for graphene on SiO$_2$[3]. These values are much higher than those for Si and GaAs sensors[14]: 100 and 700 VA^{-1} T^{-1}, respectively. Our calculations for high-quality graphene ($n_0 = 1 \times 10^{11}$ cm^{-2}, $\mu = 100{,}000$ cm^2 V^{-1} s^{-1}, $\alpha_{max} = 10\%$, $B = 2$ T, $P = 1$ mW) give $S_A^R = 4.5$ VT^{-1} which is about two times higher than the best values reported for narrow-gap III–V heterostructure sensors ($S_I = 2750$ VA^{-1} T^{-1}; $S_A = 2.17$ VT^{-1} at 1 mW)[15]. Thus, graphene provides performance much better than simple semiconductor structures and comparable to the best complex III–V heterostructure designs.

Methods

Device fabrication and characterization. Back-gated six-arm Hall bar structures were fabricated for these experiments using commercial graphene deposited by CVD and transferred to a SiO$_2$(285 nm)/p-Si substrate. Photolithography followed by oxygen plasma etching was used to pattern the graphene channel region. A

standard photoresist lift-off process was performed to form metal contacts comprised of Ti/Au (10/120 nm) layers deposited by electron beam evaporation. Examination of the current–voltage characteristics confirmed that the fabricated Hall bars exhibited excellent electrical properties (see Supplementary Fig. 3b). Raman spectroscopy was used to examine the quality of the graphene and its monolayer thickness (see Supplementary Note 3 and Supplementary Fig. 3c, d).

Transport measurements. The longitudinal resistivity ρ_{xx} and Hall resistivity ρ_{xy} were measured as a function of magnetic field B and gate-bias V_g by the van der Pauw method[34] under vacuum using a cryogenic probe Hall measurement system (Model 8425, Lake Shore Cryotronics Inc.) with a current source (Model 6220, Keithley Inc.) and a nano-voltmeter (Model 2182A, Keithley Inc.). Current-reversal averaging and geometry averaging techniques were included to remove unwanted contributions due to offset currents and offset voltages[35]. V_g was applied to the p-Si substrate and the gate leakage current was monitored. The magnetic field was applied perpendicular to the sample plane over the range of −2 to 2T and the temperature of sample stage was varied from 10 to 300 K. The temperature sensitivity observed throughout these experiments was very small, and we only present data primarily for an intermediate temperature of 100 K.

Data availability

The data that support the plots within this paper and other findings of this study are available from the corresponding author upon reasonable request.

Received: 1 November 2018 Accepted: 7 May 2019
Published online: 21 June 2019

References

1. Das Sarma, S., Adam, S., Hwang, E. H. & Rossi, E. Electronic transport in two-dimensional graphene. *Rev. Mod. Phys.* **83**, 407–470 (2011).
2. Dauber, J. et al. Ultra-sensitive Hall sensors based on graphene encapsulated in hexagonal boron nitride. *Appl. Phys. Lett.* **106**, 193501 (2015).
3. Chen, B. et al. Exploration of sensitivity limit for graphene magnetic sensors. *Carbon* **94**, 585–589 (2015).
4. Dean, C. R. et al. Boron nitride substrates for high-quality graphene electronics. *Nat. Nanotechnol.* **5**, 722–726 (2010).
5. Xu, H. et al. Batch-fabricated high-performance graphene Hall elements. *Sci. Rep.* **3**, 1207 (2013).
6. Joo, M. K. et al. Large-Scale graphene on hexagonal-BN Hall elements: prediction of sensor performance without magnetic field. *ACS Nano* **10**, 8803–8811 (2016).
7. Karpiak, B., Dankert, A. & Dash, S. P. Gate-tunable Hall sensors on large area CVD graphene protected by h-BN with 1D edge contacts. *J. Appl. Phys.* **122**, 054506 (2017).
8. Dankert, A., Karpiak, B. & Dash, S. P. Hall sensors batch-fabricated on all-CVD h-BN/graphene/h-BN heterostructures. *Sci. Rep.* **7**, 15231 (2017).
9. Huang, L., Zhang, Z., Chen, B. & Peng, L. M. Flexible graphene hall sensors with high sensitivity. in *IEEE International Electron Devices Meeting (IEDM)* 33.5.1–33.5.4 (Washington DC, USA, 2015).
10. Pisana, S., Braganca, P. M., Marinero, E. E. & Gurney, B. A. Tunable nanoscale graphene magnetometers. *Nano Lett.* **10**, 341–346 (2010).
11. Lu, J. et al. Graphene magnetoresistance device in van der Pauw geometry. *Nano Lett.* **11**, 2973–2977 (2011).
12. Gopinadhan, K. et al. Extremely large magnetoresistance in few-layer graphene/boron–nitride heterostructures. *Nat. Commun.* **6**, 8337 (2015).
13. Huang, L. et al. Ultra-sensitive graphene Hall elements. *Appl. Phys. Lett.* **104**, 183106 (2014).
14. Popovic, R. S. *Hall Effect Devices*, 2nd edn. (CRC Press, Boca Raton, FL, 2003).
15. Bando, M. et al. High sensitivity and multifunctional micro-Hall sensors fabricated using InAlSb/InAsSb/InAlSb heterostructures. *J. Appl. Phys.* **105**, 07E909 (2009).
16. Adam, S., Hwang, E. H., Galitski, V. M. & Das Sarma, S. A self-consistent theory for graphene transport. *Proc. Natl Acad. Sci. USA* **104**, 18392–18397 (2007).
17. Martin, J. et al. Observation of electron–hole puddles in graphene using a scanning single-electron transistor. *Nat. Phys.* **4**, 144–148 (2008).
18. Zhang, Y., Brar, V. W., Girit, C., Zettl, A. & Crommie, M. F. Origin of spatial charge inhomogeneity in graphene. *Nat. Phys.* 5, 722–726 (2009).
19. Hwang, E. H., Adam, S. & Das Sarma, S. Transport in chemically doped graphene in the presence of adsorbed molecules. *Phys. Rev. B.* **76**, 195421 (2007).
20. Cho, S. & Fuhrer, M. S. Charge transport and inhomogeneity near the minimum conductivity point in graphene. *Phys. Rev. B* **77**, 081402 (2008).
21. Tiwari, R. P. & Stroud, D. Model for the magnetoresistance and Hall coefficient of inhomogeneous graphene. *Phys. Rev. B* **79**, 165408 (2009).
22. Knap, M., Sau, J. D., Halperin, B. I. & Demler, E. Transport in two-dimensional disordered semimetals. *Phys. Rev. Lett.* **113**, 186801 (2014).
23. Meric, I. et al. Current saturation in zero-bandgap, top-gated graphene field-effect transistors. *Nat. Nanotechnol.* **3**, 654–659 (2008).
24. Alekseev, P. S. et al. Magnetoresistance in two-component systems. *Phys. Rev. Lett.* **114**, 156601 (2015).
25. Vasileva, G. Y. et al. Linear magnetoresistance in compensated graphene bilayer. *Phys. Rev. B* **93**, 195430 (2016).
26. Banszerus, L. et al. Ultrahigh-mobility graphene devices from chemical vapor deposition on reusable copper. *Sci. Adv.* **1**, e1500222 (2015).
27. Yamoah, M. A., Yang, W., Pop, E. & Goldhaber-Gordon, D. High-velocity saturation in graphene encapsulated by hexagonal boron nitride. *ACS Nano* **11**, 9914–9919 (2017).
28. Bolotin, K. I., Sikes, K. J., Hone, J., Stormer, H. L. & Kim, P. Temperature-dependent transport in suspended graphene. *Phys. Rev. Lett.* **101**, 096802 (2008).
29. Lee, J., Tao, L., Hao, Y., Ruoff, R. S. & Akinwande, D. Embedded-gate graphene transistors for high-mobility detachable flexible nanoelectronics. *Appl. Phys. Lett.* **100**, 152104 (2012).
30. Srivastava, P. K., Arya, S., Kumar, S. & Ghosh, S. Relativistic nature of carriers: origin of electron-hole conduction asymmetry in monolayer graphene. *Phys. Rev. B* **96**, 241407 (2017).
31. Huard, B., Stander, N., Sulpizio, J. A. & Goldhaber-Gordon, D. Evidence of the role of contacts on the observed electron-hole asymmetry in graphene. *Phys. Rev. B* **78**, 121402 (2008).
32. Farmer, D. B. et al. Chemical doping and electron−hole conduction asymmetry in graphene devices. *Nano Lett.* **9**, 388–392 (2009).
33. Hannes, W.-R., Jonson, M. & Titov, M. Electron-hole asymmetry in two-terminal graphene devices. *Phys. Rev. B* **84**, 045414 (2011).
34. van der Pauw, L. J. A method of measuring specific resistivity and Hall effect of discs of arbitrary shape. *Philips Res. Rep.* **13**, 1–9 (1958).
35. ASTM F76-08(2016)e1 Standard test methods for measuring resistivity and Hall coefficient and determining hall mobility in single-crystal semiconductors. *ASTM International* https://doi.org/10.1520/F0076-08R16E01 (West Conshohocken, PA, 2016).

Acknowledgements

The authors would like to acknowledge Z. Huang for his help in preliminary analysis of experimental data and J.R. Lindemuth (Lake Shore Cryotronics) for helpful discussions on multicarrier Hall measurements. R.K. also thanks R. Macedo for her contribution to device fabrication.

Author contributions

R.K. created and supervised the project. G.S. did most of the device fabrication and materials characterization. R.K. designed the experiments and modeling studies. G.S. and M.R. carried out the magnetotransport measurements. G.S. implemented and carried out the modeling study. G.S. and R.K. wrote the manuscript with comments from M.R.

Additional information

Supplementary information accompanies this paper at https://doi.org/10.1038/s42005-019-0161-5.

Competing interests: The authors declare no competing interests.

Reprints and permission information is available online at http://npg.nature.com/reprintsandpermissions/

Publisher's note: Springer Nature remains neutral with regard to jurisdictional claims in published maps and institutional affiliations.